Materials Advances

ROYAL SOCIETY OF CHEMISTRY

PAPER

View Article Online
View Journal | View Issue

Open Access Article. Published on 29 May 2025. Downloaded on 3/1/2026 6:22:41 PM.
This article is licensed under a Creative Commons Attribution 3.0 Unported Licence.

Check for updates

Cite this: *Mater. Adv.*, 2025, **6**, 4660

In situ synthesis of 3D ZIF-8 on 2D MXene nanosheets for efficient photocatalytic degradation of methylene blue (MB)†

Francis Ashamary,‡[ab] P. Catherine Neba,‡[ab] S. Harivarsha,‡[ab] Atchudan Raji,‡[cd] Padmanaban Annamalai,[ef] Mohamed Gamal Mohamed,‡*[gh] Pramod Kalambate,*[i] Pandi Muthirulan,[j] Shiao-Wei Kuo*[gk] and Devaraj Manoj*[ab]

Organic dyes such as methylene blue (MB), commonly discharged from the textile and paper industries, pose a serious hazard to aquatic ecosystems and human beings. Developing efficient strategies for dye degradation *via* photocatalytic processes is, therefore, of urgent importance. Metal–organic frameworks (MOFs) have emerged as promising photocatalysts owing to their high surface areas, tunable porosity, and structural diversity. However, the large band gap of pristine MOFs (typically >4.9 eV) often results in poor visible-light absorption and high charge recombination, limiting their practical applicability. Here, we report the *in situ* growth of three-dimensional zeolitic imidazolate framework-8 (ZIF-8) on two-dimensional Ti_3C_2 MXene nanosheets (ZIF-8@Ti_3C_2) *via* a facile precipitation strategy. The resulting 3D/2D hybrid architecture enhances light absorption, as confirmed by diffuse reflectance spectroscopy, and significantly narrows the band gap to 2.1 eV, substantially lower than that of pristine ZIF-8 (5.0 eV). Under visible light irradiation, the ZIF-8@Ti_3C_2 MXene heterostructure achieves a methylene blue degradation efficiency of 95% within 120 minutes, outperforming its components. This work presents a robust platform for engineering MOF-based heterostructures, offering a promising avenue toward sustainable photocatalytic water purification.

Received 9th April 2025,
Accepted 29th May 2025

DOI: 10.1039/d5ma00340g

rsc.li/materials-advances

[a] *Department of Chemistry, Karpagam Academy of Higher Education, Coimbatore 641 021, India. E-mail: manojdvrj@gmail.com*
[b] *Centre for Material Chemistry, Karpagam Academy of Higher Education, Coimbatore 641021, India*
[c] *Department of Chemistry, Saveetha School of Engineering, Saveetha Institute of Medical and Technical Sciences, Chennai 602105, Tamil Nadu, India*
[d] *School of Chemical Engineering, Yeungnam University, Gyeongsan 38541, Republic of Korea*
[e] *Facultad de Ingenieria, Universidad Catolica de la Santismia Concepcion, Concepcion 4090541, Chile*
[f] *Department of Physiology, Saveetha Institute of Medical and Technical Sciences, Chennai 600 077, India*
[g] *Department of Materials and Optoelectronic Science, Center for Functional Polymers and Supramolecular Materials, National Sun Yat-Sen University, Kaohsiung 804, Taiwan. E-mail: mgamal.eldin34@gmail.com, kuosw@faculty.nsysu.edu.tw*
[h] *Department of Chemistry, Faculty of Science, Assiut University, Assiut 71515, Egypt*
[i] *Department of Chemistry & Waterloo Institute for Nanotechnology, University of Waterloo, Waterloo, Ontario, Canada. E-mail: pkalambate@uwaterloo.ca*
[j] *Department of Chemistry, Lekshmipuram College of Arts and Science, Neyyoor-629802, India*
[k] *Department of Medicinal and Applied Chemistry, Kaohsiung Medical University, Kaohsiung 807, Taiwan*

† Electronic supplementary information (ESI) available. See DOI: **https://doi.org/10.1039/d5ma00340g**

‡ These authors equally contributed to this work.

Introduction

The textile dyeing and bleaching industry is a major contributor to water pollution, with Tiruppur in Tamil Nadu—widely recognized as the "knitwear capital of India"—serving as a central hub for such activities. These industrial units are primarily concentrated along the banks of the Noyyal river, where large volumes of synthetic dyes are routinely discharged into nearby water bodies. Commonly used dyes such as methylene blue (MB), methyl orange, rhodamine B, and Congo red represent a significant class of industrial pollutants.[1,2] According to recent statistical data released in 2024, 10 000 different types of synthetic dyes are produced globally. Among those synthetic dyes produced, 2.8 million tons of dyes are discharged into the ecosystem, which can lead to water contamination.[3–5] This unregulated discharge poses serious environmental and health risks, including degradation of water quality, disruption of aquatic biodiversity, and long-term toxicity to humans. In particular, cationic dyes like methylene blue (MB) characterized by a heterocyclic aromatic structure, are known to be persistent, and capable of obstructing sunlight penetration in water, thereby inhibiting photosynthetic activity and exacerbating

© 2025 The Author(s). Published by the Royal Society of Chemistry

Open Access Article. Published on 29 May 2025. Downloaded on 3/1/2026 6:22:41 PM. This article is licensed under a Creative Commons Attribution 3.0 Unported Licence.

ecological damage. MB can elicit a range of adverse physiological effects in humans, including cyanosis, tissue necrosis, the formation of Heinz bodies (which are indicative of oxidative damage to red blood cells), tachycardia, and other systemic disturbances. These effects arise due to MB's interactions with cellular and enzymatic processes, particularly its impact on redox reactions and hemoglobin metabolism.[6–8] A range of remediation strategies have been developed to address dye contamination in wastewater, including membrane separation, adsorption, biological treatment, ozonation, reverse osmosis, advanced oxidation processes, phytoremediation, nanotechnology, biological–chemical hybrid systems, and photodegradation.[9,10] Among these, photocatalytic degradation has gained significant attention due to its potential to mineralize dye molecules into benign end products, such as water and carbon dioxide, under ultraviolet or visible light irradiation.[11,12] Heterogeneous photocatalysis, in particular, offers practical advantages over homogeneous systems, as the solid photocatalyst can be readily separated, recovered, and reused.[13] Motivated by these advantages, a wide array of semiconductor-based materials, namely titanium dioxide (TiO_2),[14] zinc oxide (ZnO),[15] cadmium sulfide (CdS),[16] tungsten trioxide (WO_3),[17] iron oxide (Fe_2O_3),[18] nickel oxide (NiO),[19] lead halide perovskites,[20] and tin dioxide (SnO_2),[21] have been explored for photocatalytic dye degradation. However, these conventional photocatalysts often suffer from intrinsic limitations, including rapid charge carrier recombination, sluggish surface reaction kinetics, limited light absorption, catalyst leaching and aggregation, and low dye adsorption capacity, which collectively hinder their overall degradation efficiency.[22] Metal–organic frameworks (MOFs) are a class of porous crystalline materials composed of metal nodes coordinated to linkers, forming well-defined three-dimensional architectures.[23] MOFs have garnered significant attention as photocatalysts, offering advantages over conventional transition metal oxides because of their high surface area, tunable porosity, abundant active metal sites, selective adsorption and separation, high chemical and thermal stability, low density, and structural versatility.[24,25] Among them, zeolitic imidazolate frameworks (ZIFs), which belong to a subdivision of MOFs, have shown a promising dye degradation efficiency of about 87% towards dyes. However, the photocatalytic performance of pristine MOFs is reported as good or comparable with other semiconductors as photocatalysts.[26–28] This limited activity can be attributed to several intrinsic drawbacks: (1) poor dispersibility in aqueous media, (2) wide band gap values restricting visible light absorption, (3) insufficient photon-harvesting efficiency, (4) challenges in catalyst recovery and recyclability, (5) rapid recombination of photogenerated charge carriers and (6) limited chemical stability under optimal conditions.[29,30] These factors significantly hinder the practical deployment of pristine MOFs in photocatalytic water treatment. To address these limitations, MOF-based composites have been explored as an effective strategy to enhance photocatalytic efficiency through synergistic interactions.[31,32] For instance, Liaquat *et al.* synthesized a Mo@Ni-MOF composite for MB photocatalytic dye degradation. The incorporation of molybdenum (Mo) into the nickel-based metal–organic framework (Ni-MOF) significantly enhances its catalytic performance in dye degradation, achieving an efficiency of 84%; in contrast, only 68% was reported for the pristine Ni-MOF. Therefore, the MOF-based composites enhance the photocatalytic dye degradation.[33] In particular, the *in situ* growth of three-dimensional MOFs on two-dimensional (2D) substrates offers a promising approach to preserving structural integrity, which enhances structural stability, maximizes the exposure of active sites, and promotes efficient charge transport by leveraging the conductive properties of the 2D substrate.[34] To find effective conductive supports similar to graphene, MXenes particularly transition metal carbides like $Ti_3C_2T_x$ have emerged as promising 2D materials. These materials consist of early transition metals, carbon, and various surface functional groups.[35] MXenes are typically synthesized through selective etching of MAX phases, resulting in single-layer nanosheets that can serve as templates for the growth of diverse nanostructures.[36] Integrating metal–organic frameworks (MOFs) with MXene nanosheets is expected to enhance the electrical conductivity and structural stability of the MOFs. Moreover, this approach can help mitigate common issues, such as nanosheet aggregation and restacking, promoting more efficient material performance.[37] To preserve the intrinsic structural features of both the metal–organic frameworks (MOFs) and MXene nanosheets, we report the *in situ* formation of three-dimensional (3D) ZIF-8 nanostructures on two-dimensional Ti_3C_2 MXene sheets (denoted as ZIF-8@Ti_3C_2 MXene) for decolorization of MB *via* a photocatalytic pathway. The obtained hybrid architectures were systematically characterized by electron microscopy and diffraction analysis, confirming the successful integration of ZIF-8 onto the MXene surface. Under visible light irradiation, ZIF-8@Ti_3C_2 MXene exhibited significantly enhanced photocatalytic activity, achieving near-complete decolorization of methylene blue within 120 minutes—markedly outperforming pristine ZIF-8. This study highlights a versatile strategy for the rational design of MOF–MXene hybrid nanostructures, where retention of active metal sites and structural integrity is critical for functional performance.

Experimental section

Materials and methods

The chemicals and reagents used in the present work were zinc nitrate hexahydrate and 2-methylimidazole (2-MIm) from SRL Chemicals, India. Methylene blue ($C_{16}H_{18}ClN_3S$) dye was obtained from HiMedia Chemicals (India). The stock solution of the dye was prepared using double distilled (DD) water. No further purification of chemicals was carried out after purchasing.

Preparation of ZIF-8

In a typical preparation process, ZIF-8 was adopted from existing literature with slight modifications.[38] Typically, 2.97 g of zinc nitrate was weighed and allowed to dissolve in 50 mL of water to form solution I. An accurately weighed 3.28 g of 2-Mim was dissolved in another beaker containing water to form solution II. To form the MOF, solution I was added dropwise to solution II, under constant stirring, where immediate precipitation occurs.

Open Access Article. Published on 29 May 2025. Downloaded on 3/1/2026 6:22:41 PM.
This article is licensed under a Creative Commons Attribution 3.0 Unported Licence.

After complete addition, the reaction mixture was stirred for 1 min at room temperature (25 °C) and allowed to age for 24 hours.

The precipitate was collected by centrifuging at 8000 rpm using water and further subjected to washing with ethanol to remove the unreacted reactants. The samples collected were dried (60 °C) under a vacuum overnight.

Preparation of single-layered MXene nanosheets

For purification, the as-received Ti_3AlC_2 particles (2 g) were stirred continuously in 9 M HCl for 12 h and then washed and dried in an oven for 6 h at 60 °C. More specifically, 1 g of LiF was gradually added to 30 mL of 9 M HCl and vigorously agitated for 10 minutes in an oil bath at 50 °C by adding 0.75 g of MAX phase. Following 48 hours, the etched sediment was rinsed with deionized water, centrifuged for five minutes at 5500 rpm, and the supernatant was poured out. The procedure was carried out multiple times until the supernatant took on a dark green colour and its pH level was close to approximately 6. After centrifuging the suspension at 5500 rpm for five minutes, the precipitate was added to 40 mL of deionized water and manually shaken until it was redispersed entirely. This process was repeated multiple times to increase the yield of $Ti_3C_2T_x$ flakes. The MXene was collected; it was labeled as single-layered MXene and was kept in a refrigerator at 4 °C.

Synthesis of ZIF-8 @Ti_3C_2 nanosheets

For the synthesis of ZIF-8 on Ti_3C_2 nanosheets, 10 mL of MXene solution (4 mg mL^{-1}) was added into a Teflon-lined, sealed container, which is free from atmospheric oxygen to avoid oxidation. Under constant stirring, 328 mg of 2-MIm solution (32.8 mg mL^{-1}) was added dropwise at 300 rpm for 30 min to ensure positively charged 2-MIm was electrostatically attracted to the negatively charged MXene nanosheets. 297 mg of zinc nitrate solution (59.4 mg mL^{-1}) was added dropwise to the reaction mixture and stirred in an inert atmosphere. After a few minutes, precipitation occurred rapidly and it was allowed to age for 12 h. The obtained precipitate was washed with water and ethanol to remove the unreacted reactants and was dried (60 °C) under a vacuum overnight.

Preparation of dye solution and photocatalytic degradation

Initially, the MB stock solution was prepared, and the initial concentration was fixed as 1000 ppm. A series of dye concentration solutions were prepared from the initial concentration, and about 50 mL of a known concentration was transferred into a 250 mL beaker. The ZIF-8@Ti_3C_2 was weighed in various amounts, and the required weight was added to a beaker containing a dye solution. Before irradiation, the beaker was covered completely to confirm that stirring occurs in dark conditions for 30 min. This step ensures that the photocatalyst attains the adsorption/desorption equilibrium. After stirring in the dark, the solution was poured into a clean photocatalytic chamber fitted with a purging tube, which helps the uniform distribution of the catalyst throughout the experiment. For photocatalytic measurements, the light source is a 160 W Xe lamp with a wavelength of 400 to 800 nm, which was fixed in the customized photocatalytic reactor (Model: Heber-HPCR compact multi-wavelength). Once the light had been illuminated, 3 ml of the dye solution was collected, centrifuged to separate the ZIF-8 photocatalyst, and stored in vials at regular time intervals. The photo-degradation efficiency for MB was obtained from eqn (1).[39]

$$E\ (\%) = \frac{C_0 - C_t}{C_0} \times 100 \quad (1)$$

where C_0 is the absorbance coefficient for the initial concentration, and C_t represents the absorbance of MB concentration at time t following illumination.

Results and discussion

Fig. 1 illustrates the synthetic strategy for ZIF-8 and formation of ZIF-8 on the surface of Ti_3C_2 nanosheets *via* an *in situ* growth process. ZIF-8 was initially synthesized *via* a straightforward precipitation reaction by combining 2-methylimidazole and zinc nitrate in an aqueous solution. For the composite material, pre-exfoliated two-dimensional Ti_3C_2 MXene nanosheets were employed as templates for the *in situ* growth of ZIF-8 under similar reaction conditions. This synthetic pathway offers significant advantages: (i) the negatively charged terminal groups on the MXene surface facilitate the nucleation and uniform distribution of ZIF-8, while simultaneously suppressing particle agglomeration by providing abundant active sites; and (ii) strong interfacial interactions between the MXene substrate and ZIF-8 confer enhanced structural stability and integrity to the resulting hybrid. The formation and morphology of ZIF-8@Ti_3C_2 MXene nanosheets, in comparison to pristine ZIF-8, were systematically characterized to confirm the successful integration of the two components.[40] The surface morphology of ZIF-8 and the 3D ZIF-8 on the 2D Ti_3C_2 MXene hybrid was examined using FESEM. As evident from Fig. 2(a), the pristine ZIF-8 demonstrates well-defined hexagonal crystals, indicative of successful framework formation in aqueous media.[41] The nucleation and growth of ZIF-8 in the presence of 2-methylimidazole (Mim) can be attributed to the dual existence of Mim and its protonated form (Mim^+) in water, owing to its inherently high pK_a value.[42] Upon the addition of Zn^{2+} ions, coordination occurs between Zn^{2+} and Mim to form $Zn(Mim)_2^+$ complexes. The excess Mim present in the reaction medium also acts as a deprotonating agent, thereby facilitating the crystallization of ZIF-8 into its characteristic hexagonal morphology.[43] In the next step, the exfoliation of Ti_3C_2 nanosheets obtained after the etching of the MAX phase using LiF and HCl was confirmed *via* FESEM. As shown in Fig. 2(b), treatment of multilayered Ti_3C_2 with LiCl as a cationic delaminating agent under ice-cold conditions, followed by manual shaking, resulted in the formation of few-layered, two-dimensional MXene nanosheets. These nanosheets served as a template for the subsequent growth of ZIF-8. As observed in Fig. 2(c), the hybrid nanosheets are uniformly decorated with ZIF-8 nanocrystals while retaining the morphology and dispersion of the MOF particles. This suggests that the negatively charged MXene surface not only promotes the nucleation of ZIF-8 but also effectively prevents particle agglomeration, as further

 © 2025 The Author(s). Published by the Royal Society of Chemistry

Open Access Article. Published on 29 May 2025. Downloaded on 3/1/2026 6:22:41 PM.
This article is licensed under a Creative Commons Attribution 3.0 Unported Licence.

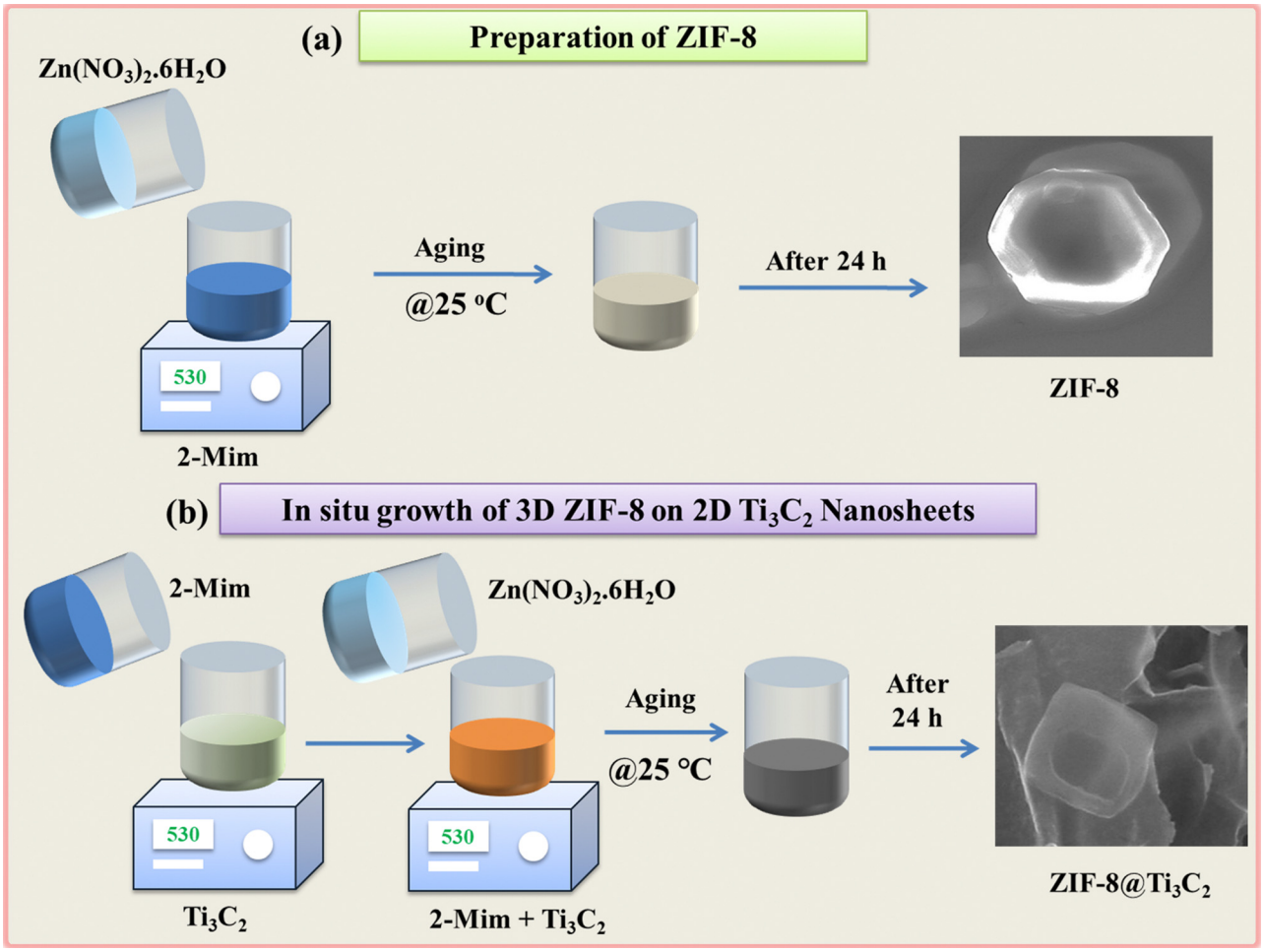

Fig. 1 Schematic representation for synthesizing (a) ZIF-8 and (b) ZIF-8@Ti_3C_2 MXene nanosheets.

corroborated by Fig. 2(d).[44] To assess the elemental composition and spatial distribution of the constituents, energy-dispersive X-ray spectroscopy (EDX) mapping was performed on the ZIF-8@Ti_3C_2 MXene hybrid [Fig. 2(e)–(h)]. The EDX spectra confirm the presence of Zn, Ti, C, and N elements, validating the successful and uniform growth of ZIF-8 on the Ti_3C_2 MXene nanosheets *via* a template-free *in situ* strategy. The present work aims to prepare ZIF-8 nanocrystals using zinc nitrate as a metal node and 2-methylimidazole as a linker, using water as a solvent. The mechanism can be explained as follows: after the addition of 2-Mim in water, reversible hydrolysis takes place and produces $[2\text{-Mim}]^+$. The addition of Zn^{2+} ions with excess addition of linker in the solution increases the pH, facilitating the deprotonation step, and leads to the formation of ZIF-8 nanocrystals. This observation further supports the solvent's role as a structure-directing agent (SDA). Therefore, water is an appropriate solvent for the formation of ZIF-8. To investigate the structural characteristics of the heterostructure photocatalyst before and after ZIF-8 deposition, X-ray diffraction (XRD) analysis was performed. The diffraction pattern of pristine ZIF-8 [Fig. 3(a)] exhibits sharp and well-defined peaks at 2θ values of 10.38°, 12.78°, 14.79°, 16.53°, and 18.08°, which correspond to the (002), (112), (022), (013), and (222) crystallographic planes, respectively. These reflections are in excellent agreement with the standard reference pattern (JCPDS no. 00-062-1030),[45] confirming the successful and phase-pure formation of ZIF-8 in the presence of 2-methylimidazole, with no detectable impurities. *In situ* formation of ZIF-8 on Ti_3C_2 MXene nanosheets was also demonstrated using XRD, and the resultant diffraction pattern displays additional peaks attributable to the MXene substrate alongside the characteristic behavior of ZIF-8. The simultaneous presence of both sets of diffraction peaks confirms the successful formation of the ZIF-8@Ti_3C_2 MXene heterostructure. Importantly, no significant shifts or broadening of the ZIF-8 peaks are observed, indicating that the crystalline framework of ZIF-8 remains intact upon integration with MXene. These observations underscore the structural compatibility and stability of the hybrid material and validate the effective formation of a well-defined heterostructure.

To investigate the functional groups, present in ZIF-8 and to confirm the successful integration of ZIF-8 onto Ti_3C_2 MXene nanosheets, Fourier-transform infrared (FTIR) spectroscopy was carried out over the spectral range of 4000–500 cm^{-1}. As shown in Fig. 3(b), the characteristic bands observed at

Open Access Article. Published on 29 May 2025. Downloaded on 3/1/2026 6:22:41 PM.
This article is licensed under a Creative Commons Attribution 3.0 Unported Licence.

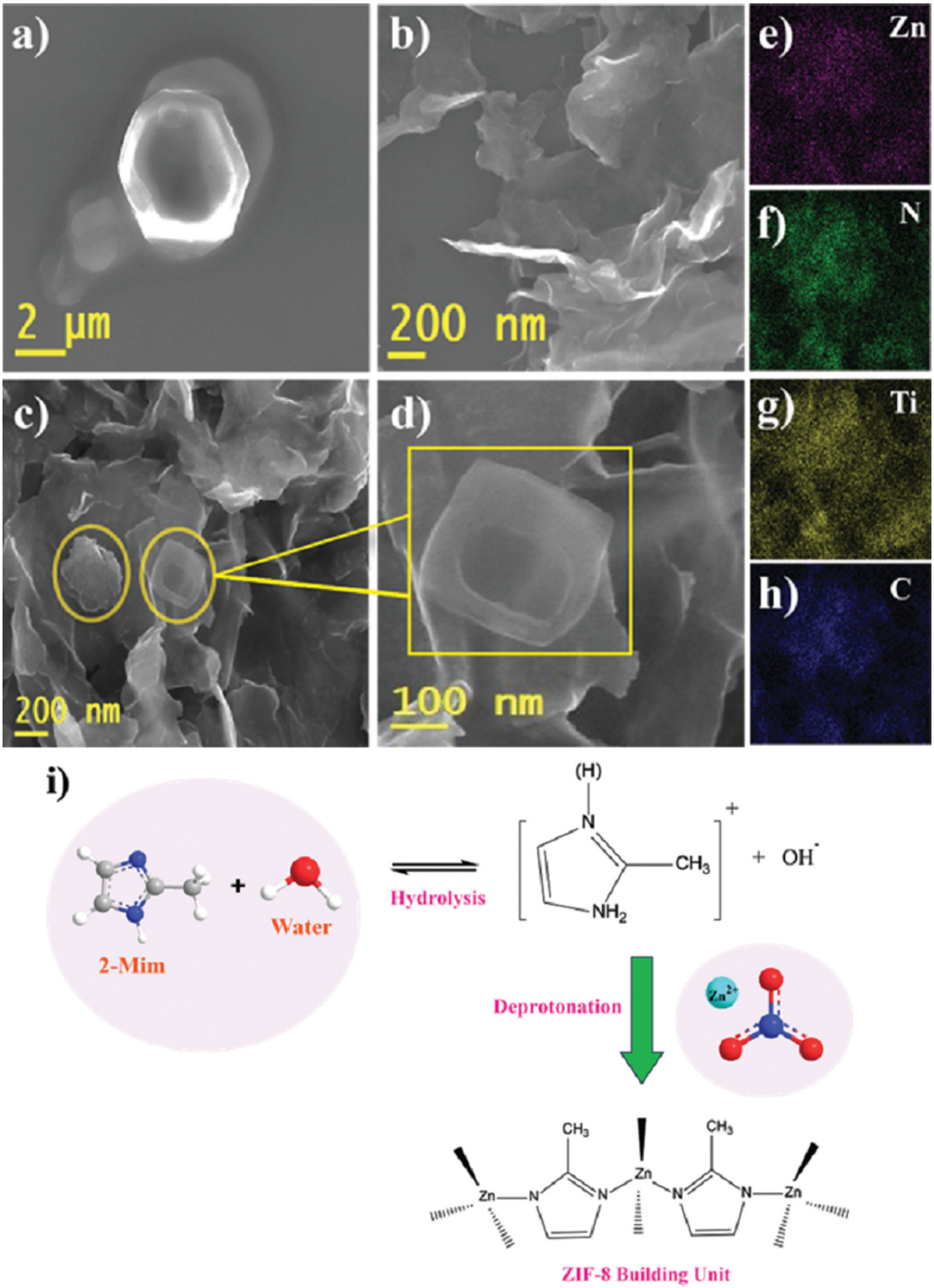

Fig. 2 SEM photographs of (a) ZIF-8, (b) Ti_3C_2 nanosheets, and (c) and (d) ZIF-8@Ti_3C_2 MXene nanosheets. (e)–(h) Elemental mapping images of ZIF-8@Ti_3C_2 MXene nanosheets. (i) Schematic representation for ZIF-8 formation in the presence of water.

1555 cm^{-1} correspond to the stretching vibration of Ti–C, and the band located at 604 cm^{-1} corresponds to bending vibrations of Ti–O, respectively, thereby confirming the formation of layered Ti_3C_2 nanosheets.[46] In the ZIF-8@Ti_3C_2 MXene hybrid, a prominent band located at 1431 cm^{-1}, attributed to the bending vibration of the methyl group in the imidazolate linker, reflects the strong coordination interaction between zinc ions and the imidazolate framework. Additional peaks at

 © 2025 The Author(s). Published by the Royal Society of Chemistry

Open Access Article. Published on 29 May 2025. Downloaded on 3/1/2026 6:22:41 PM.
This article is licensed under a Creative Commons Attribution 3.0 Unported Licence.

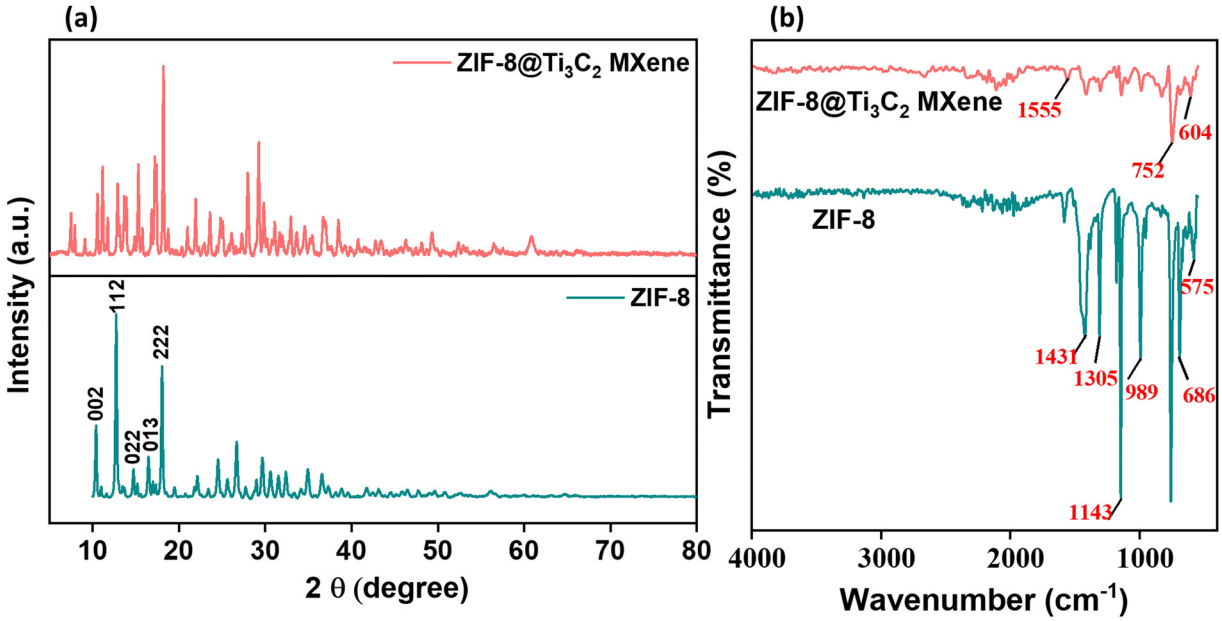

Fig. 3 (a) XRD and (b) FT-IR spectra of ZIF-8 and ZIF-8@Ti_3C_2 MXene nanosheets.

1171 and 1143 cm^{-1} arise from aromatic ring substitutions within the imidazolate moiety, suggesting coordination of Zn^{2+} to the nitrogen atom of 2-methylimidazole.[47] Due to the conformational flexibility of the linker, the nitrogen adjacent to the C3 position is preferentially involved in Zn coordination, leading to shifts in both C–C and C–H vibrational modes. A similar interaction-induced shift is observed in the C–H stretching and bending vibration at 1305 cm^{-1}.[48] The band located at 986 cm^{-1} is attributed to the stretching vibration C═N, while the bands positioned at 575, 686, and 752 cm^{-1} are associated with Zn–N and Zn–O vibrations, further confirming the incorporation of ZIF-8 onto the Ti_3C_2 surface.[49] To investigate the surface area and pore diameter of the obtained ZIF-8@MXene, BET analysis was carried out. As depicted in Fig. S1 (ESI†), the nitrogen adsorption/desorption process exhibited a type IV isotherm [Fig. S1(a), ESI†]. This can be evidenced by increased uptake of the adsorbate as the pores become filled after completion of the monolayer at higher pressure regions. The pore-size distribution [Fig. S1(b), ESI†] was calculated to be between 1.80 to 10 nm in accordance with the Barrett–Joyner–Halenda (BJH) model reflects that the synthesized ZIF-8@MXene is composed of mesopores. By adopting the multipoint Brunauer–Emmett–Teller model, the surface area of ZIF-8@MXene was calculated to be 16.2 $m^2\ g^{-1}$, and its surface area was lower than that of the ACTF@ZIF-8.[50] To estimate the optical absorption properties of pristine ZIF-8 and the ZIF-8@Ti_3C_2 MXene heterostructure, DRS-UV measurement was employed within the wavelength range of 800–200 nm. As illustrated in Fig. 4(a) and (b), ZIF-8 exhibits a relatively weak absorption edge around 305 nm, with negligible absorption in the visible region, indicating its intrinsic sensitivity to ultraviolet light. In general, for effective photocatalytic applications, materials capable of efficiently harvesting visible light are highly desirable to maximize dye degradation under solar irradiation.[51] In this context, the ZIF-8@Ti_3C_2 MXene composite displays markedly enhanced absorption across the visible region, suggesting a significant increase in its light-harvesting capability due to the integration of ZIF-8 with the conductive MXene nanosheets. This enhanced absorption implies a higher absorption coefficient compared to pristine ZIF-8. The optical band gaps of the materials were subsequently estimated using the Kubelka–Munk transformation, following eqn (2).[52]

$$(\alpha h\nu)^n = A\ (h\nu - E_g) \tag{2}$$

where h, α, A, ν, and E_g are Planck's constant, absorption coefficient, direct transition constant, light frequency, and bandgap energy, respectively. The ZIF-8@Ti_3C_2 MXene heterostructure exhibits a direct bandgap nature, corresponding to a Tauc plot exponent of $n = 2$.

In direct bandgap semiconductors, electronic excitation from the valence band to the conduction band requires comparatively less energy, facilitating more efficient charge carrier generation. As depicted in Fig. 4(c) and (d), the estimated optical bandgap energies, calculated using Tauc plots, are approximately 5.0 eV for pristine ZIF-8 and 2.1 eV for the ZIF-8@Ti_3C_2 MXene composite. This substantial reduction in bandgap upon hybridization reflects enhanced electronic coupling between the components, resulting in improved light absorption across the visible spectrum.

Furthermore, the narrowed bandgap is expected to reduce the recombination effect of photogenerated electron–hole pairs. As a result, a large improvement in separation efficiency can be achieved. Notably, as bandgap energy decreases, the photocatalyst's optical response shifts toward the visible region, aligning more closely with the solar spectrum. This enhanced visible-light absorption capability suggests that the ZIF-8@Ti_3C_2 MXene composite is a promising candidate for improved photocatalytic dye degradation in aqueous environments.

Open Access Article. Published on 29 May 2025. Downloaded on 3/1/2026 6:22:41 PM.
This article is licensed under a Creative Commons Attribution 3.0 Unported Licence.

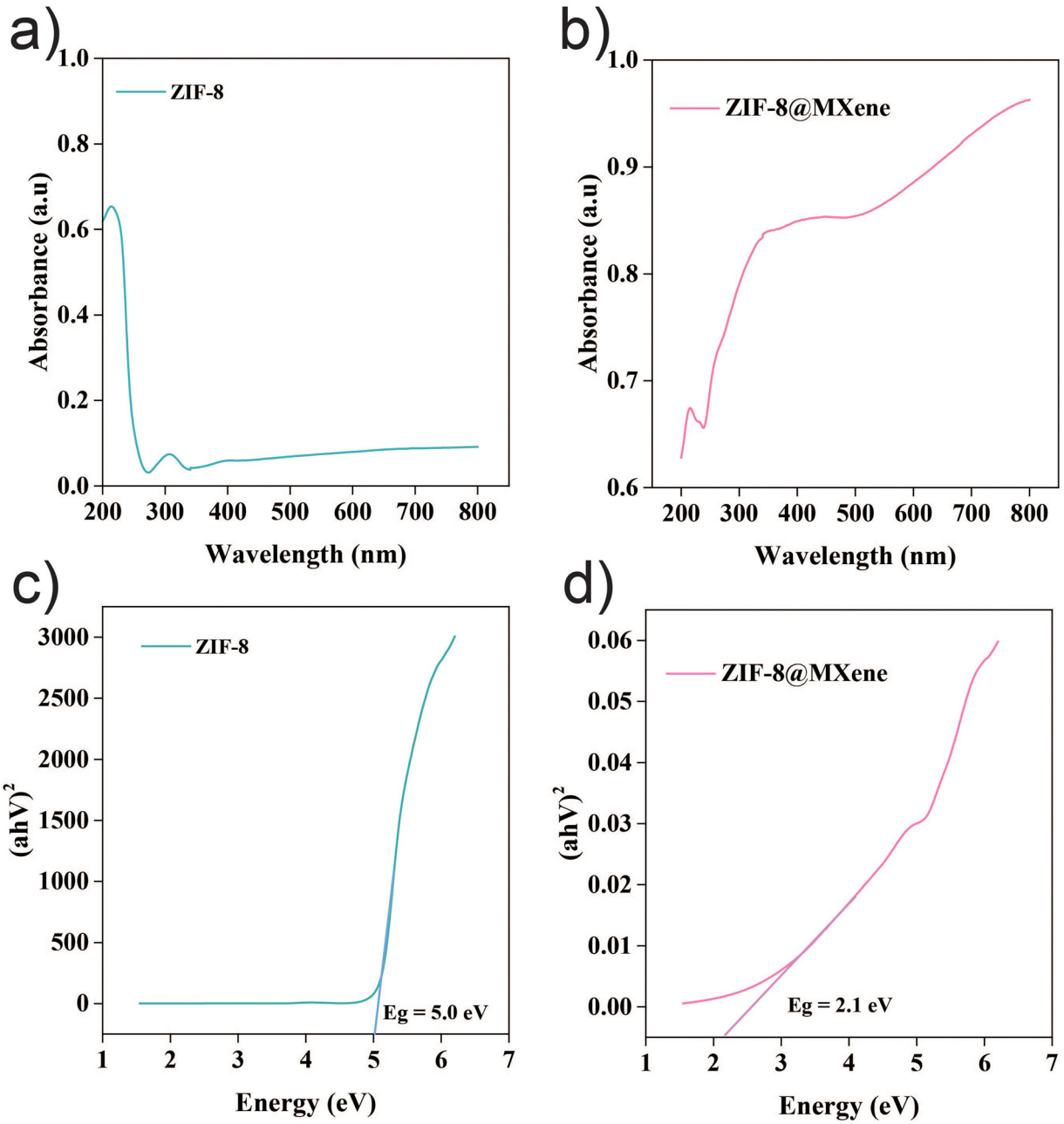

Fig. 4 (a) and (b) DRS spectra and (c) and (d) optical band gap energy (Tauc) plot of (a) and (c) ZIF-8 and (b) and (d) ZIF-8@Ti_3C_2 MXene nanosheets.

Assessment of photocatalytic activity of ZIF-8@Ti_3C_2 MXene nanosheets *via* irradiation of visible light

The photocatalytic degradation efficiency of methylene blue (MB) is largely governed by the following factors: (i) the concentration of the dye and (ii) the amount of photocatalyst dispersed in the reaction medium.[53] In this study, the initial MB concentration was fixed at 50 ppm, while the photocatalyst dosage varied between 10, 20, and 30 mg per 50 mL of solution. Upon visible-light irradiation for 120 minutes, the degradation efficiencies were determined to be approximately 56%, 95%, and 88% for catalyst loadings of 10 mg, 20 mg, and 30 mg, respectively [Fig. 5(a)–(c)]. The enhanced degradation efficiency observed with increasing photocatalyst dosage is primarily attributed to (i) the generation of a greater number of reactive oxygen species, such as hydroxyl and superoxide radicals, and (ii) increased availability of catalytically active sites on the ZIF-8@Ti_3C_2 MXene surface. However, further increasing the catalyst dosage beyond 20 mg led to a slight decrease in degradation efficiency. This decline is likely due to the aggregation of the ZIF-8@Ti_3C_2 MXene photocatalyst at higher concentrations, which decreases the number of accessible active sites and limits light penetration due to the so-called "shadow effect." The observed trend in MB decolorization indicates that the photocatalytic process proceeds *via* a heterogeneous mechanism at the

 © 2025 The Author(s). Published by the Royal Society of Chemistry

Open Access Article. Published on 29 May 2025. Downloaded on 3/1/2026 6:22:41 PM.
This article is licensed under a Creative Commons Attribution 3.0 Unported Licence.

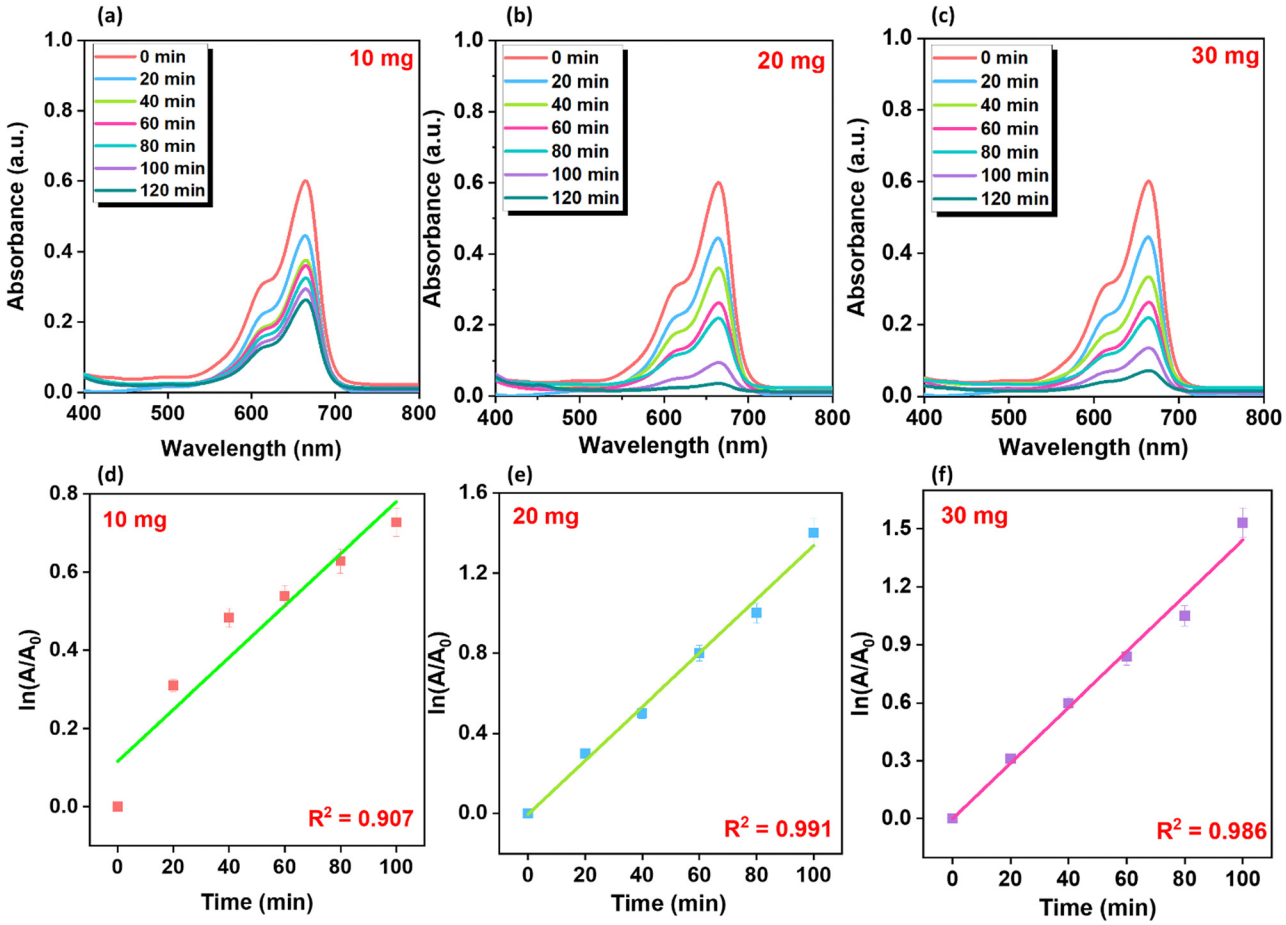

Fig. 5 Effect of ZIF-8@Ti_3C_2 MXene nanosheet photocatalyst dosage on photocatalytic performance at (a) 10 mg, (b) 20 mg, and (c) 30 mg, along with the corresponding kinetic plots for (d) 10 mg, (e) 20 mg, and (f) 30 mg.

ZIF-8@Ti_3C_2 MXene interface. Accordingly, an optimal photocatalyst loading of 20 mg was established for maximum degradation efficiency. The photocatalytic performance of the ZIF-8@Ti_3C_2 composite was investigated through the degradation of MB (MB, 50 ppm) under visible light irradiation, using 20 mg of the photocatalyst. As shown in Fig. 6(a) and (c), pristine ZIF-8 exhibited negligible changes in the absorption intensity of MB over 2 hours, indicating that it is inactive under visible light. In contrast, the ZIF-8@Ti_3C_2 MXene heterostructure displayed a markedly enhanced photocatalytic response. As shown in Fig. 6(b), an initial absorption peak at 664 nm, characteristic of MB, progressively decreased with increasing irradiation time, ultimately resulting in near complete decolorization after 120 minutes [Fig. 6(d)].

The degradation efficiency of MB using ZIF-8@Ti_3C_2 MXene was determined to be approximately 95%, calculated according to eqn (1). This high photocatalytic activity under visible light can be attributed to the generation of reactive charge carriers upon photoexcitation of the ZIF-8@Ti_3C_2 MXene composite. The synergistic interaction between the photoactive ZIF-8 framework and the conductive Ti_3C_2 MXene sheets facilitates efficient charge separation and transfer, thereby promoting the formation of reactive oxygen species responsible for the photodegradation of the dye. Kinetic analysis provides critical insights into the underlying chemical pathways governing photocatalytic degradation processes. To elucidate the reaction kinetics of MB photodegradation, a photo-Fenton-like mechanism was evaluated using widely applied kinetic models, namely pseudo-first-order and pseudo-second-order, as described in eqn (3) and (4), respectively.[54]

$$\ln \frac{A_0}{A} = kt \tag{3}$$

$$\frac{1}{A} + \frac{1}{A_0} = kt \tag{4}$$

where k is the reaction's rate constant, A_0 is the initial concentration of MB dye, and A is the dye solution's concentration at time t. From Fig. 5(d)–(f), it has been found that ZIF-8@Ti_3C_2 MXene follows a pseudo-first-order kinetic pathway, and the correlation coefficient was calculated to be R^2 = 0.991. The following eqn (5) provides the pseudo-first order linearized integrated rate law.[55]

$$\ln (A_0/A) = k_{app} \times t \tag{5}$$

where k_{app} is the apparent rate derived from a linear relationship between ln $(A_0 - A)$ and time (t), A_0 is the initial

Open Access Article. Published on 29 May 2025. Downloaded on 3/1/2026 6:22:41 PM.
This article is licensed under a Creative Commons Attribution 3.0 Unported Licence.

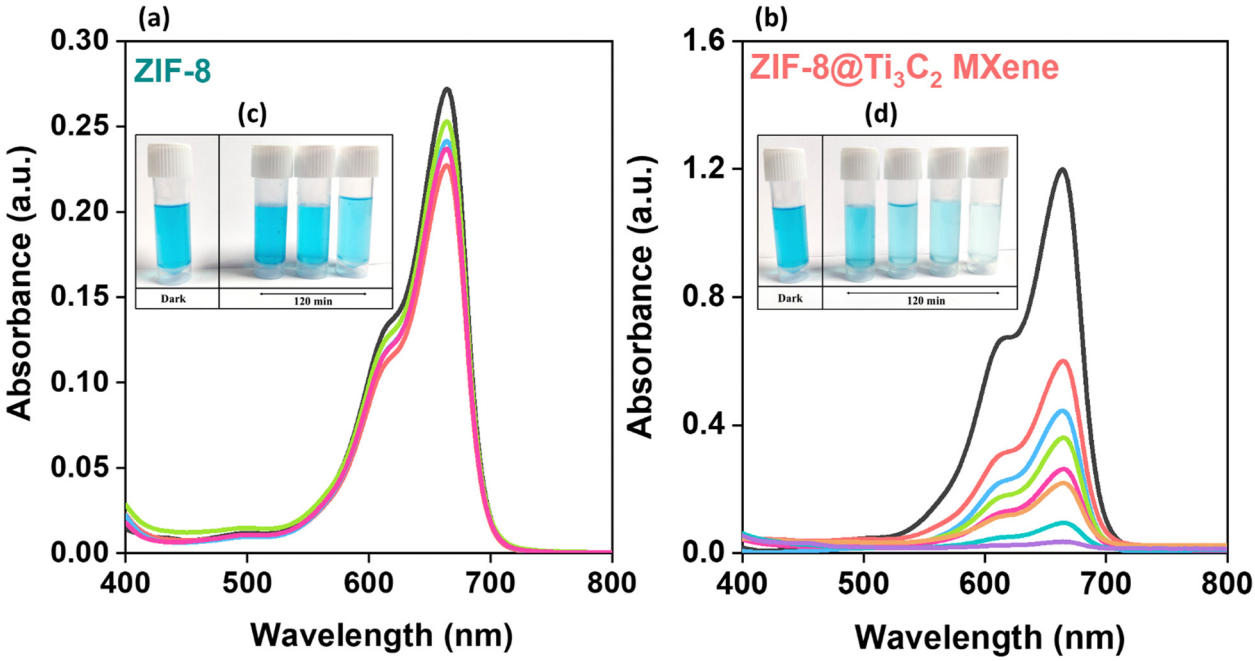

Fig. 6 Photocatalytic dye degradation of ZIF-8 (a) and ZIF-8@Ti_3C_2 MXene nanosheets (b). Corresponding photographs of dye degradation under visible light irradiation for (c) ZIF-8 and (d) ZIF-8@Ti_3C_2 MXene nanosheets.

concentration, and A is the change in concentration of MB concerning time. For MB photodegradation, the ZIF-8@Ti_3C_2 MXene composite of 20 mg had a respective apparent rate constant (k_{app}) of 0.01343 min^{-1}. To evaluate the repeatability and stability of the photocatalytic degradation performance of ZIF-8@Ti_3C_2 MXene, recycling experiments were conducted under identical conditions across four independent photocatalytic chambers. In each cycle, ZIF-8@Ti_3C_2 MXene was employed as the photocatalyst for the decolorization of methylene blue (MB). As illustrated in Fig. S2 (ESI†), the obtained ZIF-8@MXene consistently demonstrates high photocatalytic efficiency across all trials. The relative standard deviation (RSD) towards the degradation efficiency of MB under various repeatable experiments was calculated to be 2.4%, indicating excellent reproducibility and stability of the ZIF-8@Ti_3C_2 MXene photocatalyst. Table S1 (ESI†) reveals that the ZIF-8@Ti_3C_2 MXene nanosheets exhibit superior photocatalytic activity for the degradation of MB, outperforming many previously reported materials in both efficiency and degradation kinetics.

Mechanism of MB photo-degradation

The enhanced photocatalytic performance and underlying mechanism of the ZIF-8@Ti_3C_2 MXene heterostructure are illustrated schematically in Fig. 7. ZIF-8, a wide-bandgap semiconductor, can absorb photons with energies exceeding its optical bandgap, promoting electrons from the valence band (VB) to the conduction band (CB) and thereby generating photogenerated electron–hole (e^-–h^+) pairs.[56] These charge carriers drive redox reactions at the catalyst surface: photogenerated electrons reduce adsorbed O_2 molecules to superoxide radicals ($^{\bullet}O_2^-$), while holes oxidize water molecules to generate reactive hydroxyl radicals ($^{\bullet}OH$).[57,58] Both of them play a vital role in the photocatalytic degradation of MB. The formation of a heterojunction between ZIF-8 and Ti_3C_2 MXene facilitates interfacial charge transfer, whereby electrons migrate from the CB of ZIF-8 to the conductive Ti_3C_2 nanosheets. This process not only suppresses the rapid recombination of e^-–h^+ pairs but may also modulate the electronic band structure of the composite, contributing to a narrowed effective bandgap.[59] Additionally, the plasmonic-like behavior of Ti_3C_2 enables the excitation of high-energy "hot electrons" under light irradiation, which can further transfer to ZIF-8 and enhance the generation of $^{\bullet}OH$ radicals.[60] Collectively, the ZIF-8@Ti_3C_2 MXene heterostructure exhibits prolonged carrier lifetimes and more efficient charge separation, leading to increased formation of reactive oxygen species (ROS) such as $^{\bullet}O_2^-$ and $^{\bullet}OH$. These synergistic effects significantly enhance the degradation of organic pollutants *via* the photocatalytic pathway.

Conclusions

In summary, a ZIF-8@Ti_3C_2 MXene composite was successfully synthesized *via* a one-pot or *in situ* formation approach, resulting in a well-integrated heterostructure. Under visible light irradiation, the photocatalytic degradation of MB obeyed pseudo-first-order kinetics, and the relative apparent rate constant was 0.01343 min^{-1}. The ZIF-8@Ti_3C_2 MXene composite exhibited enhanced absorption in the visible zonal region and achieved a high degradation efficiency of 95% within 120 minutes. This marked improvement in photocatalytic performance is attributed to the synergistic interaction between the ZIF-8 framework and the Ti_3C_2 nanosheet, which facilitates

 © 2025 The Author(s). Published by the Royal Society of Chemistry

Open Access Article. Published on 29 May 2025. Downloaded on 3/1/2026 6:22:41 PM.
This article is licensed under a Creative Commons Attribution 3.0 Unported Licence.

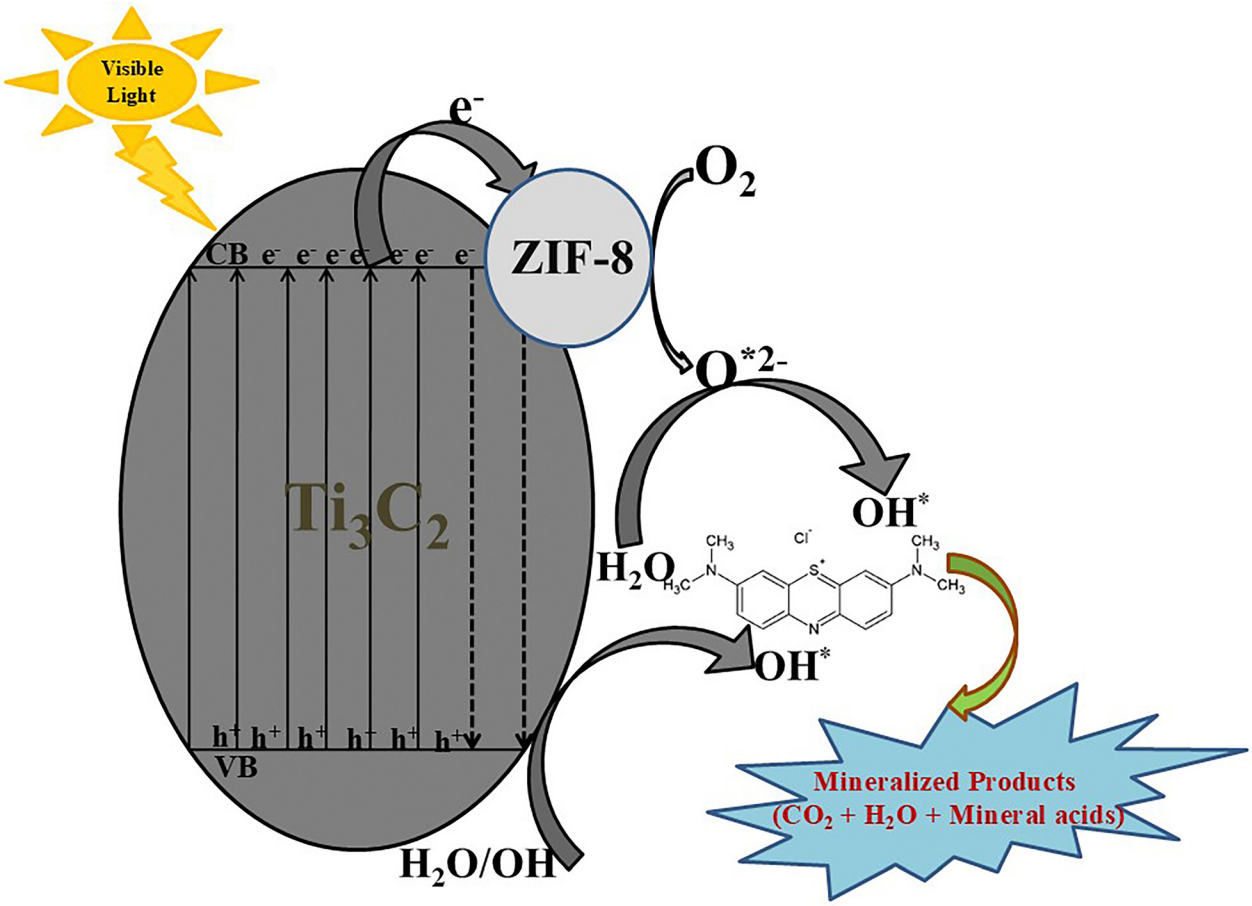

Fig. 7 Schematic representation of the degradation mechanism of MB using ZIF-8@Ti_3C_2 MXene nanosheets.

efficient charge separation and visible light utilization. These results highlight the potential of MOF-based heterostructures anchored on two-dimensional nanosheets as promising candidates for the development of efficient photocatalysts. Such materials offer a compelling alternative to conventional photocatalysts for dye degradation under visible light and may pave the way for advanced strategies in environmental remediation.

Author contributions

Francis Ashamary: investigation, methodology, conceptualization, writing – original draft. P. Catherine Neba: investigation, methodology, conceptualization, writing – original draft. S. Harivarsha: investigation, methodology, conceptualization, writing–original draft. Atchudan Raji: investigation, methodology, conceptualization, writing – original draft. Padmanaban Annamalai: investigation, methodology, Mohamed Gamal Mohamed: investigation, methodology, conceptualization, supervision, writing – original draft. Pramod Kalambate: supervision, writing – original draft. Pandi Muthirulan: investigation. Shiao-Wei Kuo: supervision. Devaraj Manoj: investigation, methodology, conceptualization, supervision, writing – original draft.

Data availability

Data is contained within the article or ESI.†

Conflicts of interest

There are no conflicts to declare.

Acknowledgements

The author (S. R.) acknowledges the support of ANID through the project Fondecyt regular N.1220663. This study was supported financially by the National Science and Technology Council, Taiwan, under contracts NSTC 112-2223-E-110-002- and 112-2218-E-110-007.

Notes and references

1 M. G. Mohamed, A. M. Elewa, N. P. Chen, A. A. K. Mohammed and S. W. Kuo, *Colloids Surf., A*, 2025, **721**, 137214, DOI: 10.1016/j.colsurfa.2025.137214.
2 H. Saadi, E. H. Atmani and N. Fazouan, *Environ. Prog. Sustainable Energy*, 2025, **44**, e14529, DOI: 10.1002/ep.14529.

Open Access Article. Published on 29 May 2025. Downloaded on 3/1/2026 6:22:41 PM.
This article is licensed under a Creative Commons Attribution 3.0 Unported Licence.

3 A. A. E. A. Elfiky, M. F. Mubarak, M. Keshawy, I. E. T. E. Sayed and T. A. Moghny, *Environ. Dev. Sustain.*, 2023, **26**, 19935–19957, DOI: 10.1007/s10668-023-03444-1.
4 B. Lellis, C. Z. Fávaro-Polonio, J. A. Pamphile and J. C. Polonio, *Biotechnol. Res. Innov.*, 2019, **3**, 275–290, DOI: 10.1016/j.biori.2019.09.001.
5 H. B. Slama, A. Chenari Bouket, Z. Pourhassan, F. N. Alenezi, A. Silini, H. Cherif-Silini, T. Oszako, L. Luptakova, P. Golińska and L. Belbahri, *Appl. Sci.*, 2021, **11**, 6255, DOI: 10.3390/app11146255.
6 M. F. Mubarak, H. Selim, H. B. Hawash and M. Hemdan, *Environ. Sci. Pollut. Res.*, 2023, **31**, 2297–2313, DOI: 10.1007/s11356-023-31240-x.
7 P. O. Oladoye, T. O. Ajiboye, E. O. Omotola and O. J. Oyewola, *Res. Eng.*, 2022, **16**, 100678, DOI: 10.1016/j.rineng.2022.100678.
8 A. Sahu and J. C. Poler, *J. Environ. Chem. Eng.*, 2024, **12**, 113754, DOI: 10.1016/j.jece.2024.113754.
9 P. O. Oladoye, M. Kadhom, I. Khan, K. H. H. Aziz and Y. A. Alli, *Green Chem. Eng.*, 2024, **5**, 440–460, DOI: 10.1016/j.gce.2023.12.004.
10 C. Kathing and G. Saini, *Recent Prog. Mater.*, 2022, **4**, 1–15, DOI: 10.21926/rpm.2204028.
11 S. M. Anisuzzaman, C. G. Joseph, C. K. Pang, N. A. Affandi, S. N. Maruja and V. Vijayan, *Chem. Eng.*, 2022, **6**, 58, DOI: 10.3390/chemengineering6040058.
12 W. Mohammed, M. Matalkeh, R. M. Al Soubaihi, A. Elzatahry and K. M. Saoud, *ACS Omega*, 2023, **8**, 40063–40077, DOI: 10.1021/acsomega.3c01766.
13 D. Friedmann, *Water*, 2022, **14**, 3588, DOI: 10.3390/w14213588.
14 L. Soares and A. Alves, *Mater. Lett.*, 2018, **211**, 339–342, DOI: 10.1016/j.matlet.2017.10.023.
15 Manikanika and L. Chopra, *Mater. Today: Proc.*, 2022, **52**, 1653–1656, DOI: 10.1016/j.matpr.2021.11.283.
16 S. Hamdan, K. Al-Ali, L. F. Vega, M. Muscetta, A. O. Yusuf and G. Palmisano, *J. Environ. Chem. Eng.*, 2024, **12**, 113937, DOI: 10.1016/j.jece.2024.113937.
17 O. Samuel, M. H. D. Othman, R. Kamaludin, O. Sinsamphanh, H. Abdullah, M. H. Puteh and T. A. Kurniawan, *Ceram. Int.*, 2022, **48**, 5845–5875, DOI: 10.1016/j.ceramint.2021.11.158.
18 A. Halfadji, A. Chougui, R. Djeradi, F. Z. Ouabad, H. Aoudia and S. Rajendrachari, *ACS Omega*, 2023, **8**, 39907–39916, DOI: 10.1021/acsomega.3c06420.
19 A. Akbari, Z. Sabouri, H. A. Hosseini, A. Hashemzadeh, M. Khatami and M. Darroudi, *Inorg. Chem. Commun.*, 2020, **115**, 107867, DOI: 10.1016/j.inoche.2020.107867.
20 Y. Huang, J. Yu, Z. Wu, B. Li and M. Li, *RSC Adv.*, 2024, **14**, 4946–4965, DOI: 10.1039/d3ra07998h.
21 K. Vinodgopal, I. Bedja and P. V. Kamat, *Chem. Mater.*, 1996, **8**, 2180–2187, DOI: 10.1021/cm950425y.
22 Z. Zheng, J. He, Z. Zhang, A. Kumar, M. Khan, C. W. Lung and I. M. C. Lo, *Environ. Sci.: Nano*, 2024, **11**, 1784–1816, DOI: 10.1039/d3en00906h.
23 E. Sivasurya, R. Atchudan, M. G. Mohamed, A. Thangamani, S. Rajendran, A. Jalil, P. K. Kalambate, D. Manoj and S.-W. Kuo, *Mater. Today Chem.*, 2025, **44**, 102538, DOI: 10.1016/j.mtchem.2025.102538.
24 A. H. Ragab, N. F. Gumaah, A. A. El Aziz Elfiky and M. F. Mubarak, *BMC Chem.*, 2024, **18**, 121, DOI: 10.1186/s13065-024-01211-5.
25 F. Sher, A. Hayward, A. E. Guerraf, B. Wang, I. Ziani, H. Hrnjić, E. Boškailo, A. Chupin and M. R. Nemţanu, *J. Mater. Chem. A*, 2024, **12**, 27932–27973, DOI: 10.1039/d4ta03877k.
26 W.-T. Chung, I. M. A. Mekhemer, M. G. Mohamed, A. M. Elewa, A. F. M. EL-Mahdy, H.-H. Chou, S.-W. Kuo and K. C.-W. Wu, *Coord. Chem. Rev.*, 2023, **483**, 215066, DOI: 10.1016/j.ccr.2023.215066.
27 L. E. Mphuthi, E. Erasmus and E. H. G. Langner, *ACS Omega*, 2021, **6**, 31632–31645, DOI: 10.1021/acsomega.1c04142.
28 X.-S. Li, Y.-J. He, J. Chen, Q.-Q. Li, P. Liu and J.-L. Li, *Inorg. Chem. Front.*, 2024, **11**, 6794–6852, DOI: 10.1039/d4qi01449a.
29 M. F. Mubarak, G. E. Khedr and H. M. El Sharkawy, *J. Alloys Compd.*, 2024, **1000**, 175151, DOI: 10.1016/j.jallcom.2024.175151.
30 M. S. Khan, Y. Li, D.-S. Li, J. Qiu, X. Xu and H. Y. Yang, *Nanoscale Adv.*, 2023, **5**, 6318–6348, DOI: 10.1039/d3na00627a.
31 Y. Gogotsi and Q. Huang, *ACS Nano*, 2021, **15**, 5775–5780, DOI: 10.1021/acsnano.1c03161.
32 M. Alhabeb, K. Maleski, B. Anasori, P. Lelyukh, L. Clark, S. Sin and Y. Gogotsi, *Chem. Mater.*, 2017, **29**, 7633–7644, DOI: 10.1021/acs.chemmater.7b02847.
33 R. Liaqat, M. Jamshaid, H. M. Abo-Dief, S. E. Ali, Z. M. El-Bahy, M. Fiaz, M. A. Wattoo and A. U. Rehman, *J. Mol. Struct.*, 2024, **1315**, 139011, DOI: 10.1016/j.molstruc.2024.139011.
34 C. Chen, L. Shen, B. Wang, X. Lu, S. Raza, J. Xu, B. Li, H. Lin and B. Chen, *Chem. Soc. Rev.*, 2025, **54**, 2208–2245, DOI: 10.1039/D4CS00435C.
35 H. Yang, G.-X. Zhang, H.-J. Zhou, Y.-Y. Sun and H. Pang, *Energy Mater. Adv.*, 2023, **4**, 0033, DOI: 10.34133/energymatadv.0033.
36 H.-P. Jing, C.-C. Wang, Y.-W. Zhang, P. Wang and R. Li, *RSC Adv.*, 2014, **4**, 54454–54462, DOI: 10.1039/c4ra08820d.
37 R. M. Mohamed, I. A. Mkhalid, E. S. Baeissa and M. A. Al-Rayyani, *J. Nanotechnol.*, 2012, **2012**, 1–5, DOI: 10.1155/2012/329082.
38 J. Liu, S. Chen, W. Shang, J. Ma and J. Zhang, *Adv. Funct. Mater.*, 2025, 2422081, DOI: 10.1002/adfm.202422081.
39 P. D. Du, N. T. Hieu and T. V. Thien, *J. Nanomater.*, 2021, **2021**, 1–12, DOI: 10.1155/2021/9988998.
40 Y. Zhang, Y. Jia, M. Li and L. Hou, *Sci. Rep.*, 2018, **8**, 9597, DOI: 10.1038/s41598-018-28015-7.
41 J. Łuczak, M. Kroczewska, M. Baluk, J. Sowik, P. Mazierski and A. Zaleska-Medynska, *Adv. Colloid Interface Sci.*, 2023, **314**, 102864, DOI: 10.1016/j.cis.2023.102864.
42 S. Iravani, E. N. Zare, A. Zarrabi, A. Khosravi and P. Makvandi, *FlatChem*, 2024, **44**, 100631, DOI: 10.1016/j.flatc.2024.100631.
43 Y. Sun, H. Zhang, Y. Lv, S. An and R. Wang, *RSC Adv.*, 2024, **14**, 17498–17506, DOI: 10.1039/d4ra02548b.
44 T. Parker, D. Zhang, D. Bugallo, K. Shevchuk, M. Downes, G. Valurouthu, A. Inman, B. Chacon, T. Zhang, C. E. Shuck, Y.-J. Hu and Y. Gogotsi, *Chem. Mater.*, 2024, **36**, 8437–8446, DOI: 10.1021/acs.chemmater.4c01536.
45 T. Truong, T. M. Hoang, C. K. Nguyen, Q. T. N. Huynh and N. T. S. Phan, *RSC Adv.*, 2015, **5**, 24769–24776, DOI: 10.1039/C4RA16168H.

 © 2025 The Author(s). Published by the Royal Society of Chemistry

Open Access Article. Published on 29 May 2025. Downloaded on 3/1/2026 6:22:41 PM.
This article is licensed under a Creative Commons Attribution 3.0 Unported Licence.

46 A. H. A. Rahim, S. N. F. Yusuf, S. R. Majid and Z. Osman, *J. Appl. Electrochem.*, 2022, **52**, 159–172, DOI: 10.1007/s10800-021-01627-0.
47 D. Huang, Q. Xin, Y. Ni, Y. Shuai, S. Wang, Y. Li, H. Ye, L. Lin, X. Ding and Y. Zhang, *RSC Adv.*, 2018, **8**, 6099–6109, DOI: 10.1039/c7ra09794h.
48 M. Lv, L. Yang, X. Wang, X. Cheng, Y. Song, Y. Yin, H. Liu, Y. Han, K. Cao, W. Ma, G. Qi and S. Li, *RSC Adv.*, 2019, **9**, 40694–40707, DOI: 10.1039/c9ra07562c.
49 P. Makuła, M. Pacia and W. Macyk, *J. Phys. Chem. Lett.*, 2018, **9**, 6814–6817, DOI: 10.1021/acs.jpclett.8b02892.
50 M. Hemdan, A. H. Ragab, S. S. Elyan, M. A. Taher and M. F. Mubarak, *J. Cluster Sci.*, 2025, **36**, 2, DOI: 10.1007/s10876-024-02730-w.
51 Z. Kalaycıoğlu, B. Özuğur Uysal, Ö. Pekcan and F. B. Erim, *ACS Omega*, 2023, **8**, 13004–13015, DOI: 10.1021/acsomega.3c00198.
52 J. Darabdhara, S. Roy and Md Ahmaruzzaman, *Inorg. Chem. Commun.*, 2023, **152**, 110694, DOI: 10.1016/j.inoche.2023.110694.
53 Z. Tian, Z. Hou, X. Yang, L. Liu and W. Zhang, *Adv. Eng. Mater.*, 2023, **25**, 2201710, DOI: 10.1002/adem.202201710.
54 M. El Ouardi, A. El Aouni, H. Ait Ahsaine, M. Zbair, A. BaQais and M. Saadi, *Chemosphere*, 2022, **308**, 136483, DOI: 10.1016/j.chemosphere.2022.136483.
55 M. Kumari and M. Pulimi, *ACS Omega*, 2023, **8**, 34262–34280, DOI: 10.1021/acsomega.3c02977.
56 L. G. Trung, M. K. Nguyen, T. D. H. Nguyen, V. A. Tran, J. S. Gwag and N. T. Tran, *RSC Adv.*, 2023, **13**, 5908–5924, DOI: 10.1039/d2ra08312d.
57 Y. Nosaka and A. Nosaka, *ACS Energy Lett.*, 2016, **1**, 356–359, DOI: 10.1021/acsenergylett.6b00174.
58 M. Ejaz, M. G. Mohamed, M. G. Kotp, A. M. Elewa and S. W. Kuo, *Colloids Surf., A*, 2025, 137239, DOI: 10.1016/j.colsurfa.2025.137239.
59 M. A. Ahmed, S. A. Mahmoud and A. A. Mohamed, *RSC Adv.*, 2025, **15**, 15561–15603, DOI: 10.1039/D4RA08780A.
60 B. Zhang, Y. Wang, Z. Wang, G. Tan, T. Liu, S. Feng, Y. Tan, W. Liu, Q. Yang, Y. Liu, A. Xia, H. Ren and Y. Wu, *Appl. Catal., B*, 2023, **339**, 123132, DOI: 10.1016/j.apcatb.2023.123132.